# On the Rapid Intensification of Hurricane Wilma (2005). Part II: Convective Bursts and the Upper-Level Warm Core

HUA CHEN AND DA-LIN ZHANG

*Department of Atmospheric and Oceanic Science, University of Maryland, College Park, College Park, Maryland*

(Manuscript received 22 February 2012, in final form 30 July 2012)

## ABSTRACT

Previous studies have focused mostly on the roles of environmental factors in the rapid intensification (RI) of tropical cyclones (TCs) because of the lack of high-resolution data in inner-core regions. In this study, the RI of TCs is examined by analyzing the relationship between an upper-level warm core, convective bursts (CBs), sea surface temperature (SST), and surface pressure falls from 72-h cloud-permitting predictions of Hurricane Wilma (2005) with the finest grid size of 1 km. Results show that both the upper-level inertial stability increases and static stability decreases sharply 2–3 h prior to RI, and that the formation of an upper-level warm core, from the subsidence of stratospheric air associated with the detrainment of CBs, coincides with the onset of RI. It is found that the development of CBs precedes RI, but most subsidence warming radiates away by gravity waves and storm-relative flows. In contrast, many fewer CBs occur during RI, but more subsidence warming contributes to the balanced upper-level cyclonic circulation in the warm-core (as intense as 20°C) region. Furthermore, considerable CB activity can still take place in the outer eyewall as the storm weakens during its eyewall replacement. A sensitivity simulation, in which SSTs are reduced by 1°C, shows pronounced reductions in the upper-level warm-core intensity and CB activity. It is concluded that significant CB activity in the inner-core regions is an important ingredient in generating the upper-level warm core that is hydrostatically more efficient for the RI of TCs, given all of the other favorable environmental conditions.

## 1. Introduction

Although there have been some improvements in tropical cyclone (TC) intensity forecasts in recent years (Rappaport et al. 2009), our ability to understand and predict the rapid intensification (RI) of TCs is very limited because of the lack of high-resolution data, where RI is defined as a deepening rate of greater than 42 hPa day$^{-1}$ (or 1.75 hPa h$^{-1}$) in the minimum central pressure $P_{\mathrm{MIN}}$ by Holliday and Thompson (1979) for western Pacific TCs or 15 m s$^{-1}$ day$^{-1}$ in the surface maximum tangential wind $V_{\mathrm{MAX}}$ by Kaplan and DeMaria (2003) for Atlantic TCs. Previous studies have focused mostly on the roles of environmental factors in RI, such as sea surface temperature (SST), vertical wind shear (VWS), and relative humidity in the lower troposphere. Obviously, these factors are not much different from those favoring tropical cyclogenesis or normal TC intensification. Thus, it is highly desirable to identify some storm characteristics, particularly inner-core processes, that distinguish the periods of RI from those occurring in the more frequently observed non-RI periods.

Gray (1998) finds that even when all favorable environmental factors are present, TCs would not intensify without outbreaks of organized deep convection. His study singles out the important roles of convective-scale process in spinning up a preexisting TC vortex from a large-scale disturbance, such as an African easterly wave or a monsoon trough. The outbreaks of deep convection have been given great attention with different terms since the work of Gentry et al. (1970), who identified them from cold brightness temperatures in satellite images and recognized their significance in TC intensification. They were termed as ''circular exhaust clouds'' by Gentry et al. (1970), extreme convection by Gray (1998), and convective bursts (CBs) or ''hot towers'' by many other studies (e.g., Steranka et al. 1986; Rodgers et al. 1998; Heymsfield et al. 2001; Guimond et al. 2010). In this study, we will use the

---

*Corresponding author address:* Dr. Da-Lin Zhang, Department of Atmospheric and Oceanic Science, University of Maryland, College Park, 2419 CSS Building, College Park, MD 20742-2425.
E-mail: dalin@atmos.umd.edu

DOI: 10.1175/JAS-D-12-062.1

more common term, that is, CB, which is defined herein as a deep, intense convective system consisting of one or more updrafts of at least 15 m $s^{-1}$ in the upper troposphere (i.e., typically above $z$ = 11 km) that are resolvable by the model finest grid size. These individual intense updrafts, referred to as CB elements, are not resolvable by satellite images but may be inferred from lightning data since more lightning occurs in extremely tall convective towers (Kelley et al. 2004). Observations show the development of CBs preceding RI or coinciding with the onset of RI (Rodgers et al. 1998, 2000; Price et al. 2009; Guimond et al. 2010; Fierro and Reisner 2011), and few occurrences of CBs when TCs reach a quasi-steady state or start weakening (Molinari et al. 1999).

Several hypotheses have been put forward on the roles of CBs in the RI of TCs. Nolan (2007) and Montgomery et al. (2006) propose that the roles of CBs are to moisten the midtroposphere such that deep convection can occur symmetrically in the eyewall, leading to the more rapid contraction of TCs. Reasor et al. (2009) find that the upper-level updrafts and reflectivity wrap around the eye into a more axisymmetric pattern as each CB intensifies and rotates into the upshear quadrants during the RI of Hurricane Guillermo (1997). Some earlier studies have documented significant subsidence warming flanking intense updrafts that penetrate into high altitudes (Velden and Smith 1983; Foley 1998; Holland et al. 1984; Rogers et al. 2002). Heymsfield et al. (2001) show the generation of an eye 6 h after some CBs overshoot into the lower stratosphere, and their results suggest that the associated compensating subsidence contributes to the formation of a warm core and the intensification of Hurricane Bonnie (1998). By analyzing an episode of CBs preceding the RI of Hurricane Dennis (2005), Guimond et al. (2010) conclude that the accumulative effects of intense downdrafts of 10–12 m $s^{-1}$ flanking CBs with the maximum updraft of 20 m $s^{-1}$ at 12–14-km height account for the increased warm-core intensity. Clearly, the more intense the warm core, the greater will be the hydrostatically induced surface pressure falls.

More importantly, it is well known from the hydrostatic equation that a higher-level warm core will cause a greater surface pressure fall than a lower-level one because of the more amplifying effects of the upper-level warming (Malkus and Riehl 1960; Zhang and Fritsch 1988; Hirschberg and Fritsch 1993; Holland 1997). However, previous observational and modeling studies have shown the formation of the warm core at different heights, varying from 600 to 200 hPa (LaSeur and Hawkins 1963; Hawkins and Rubsam 1968; Hawkins and Imbembo 1976; Liu et al. 1997). Thus, the reason why the warm core develops at different heights and what process determines the height remains elusive. In particular, we have not obtained a well-accepted theory to explain the eye subsidence generating the warm core [see the related discussion in Zhang et al. (2000) and Zhang and Kieu (2006)].

In Chen et al. (2011, hereafter Part I), we have successfully obtained a 72-h (i.e., 0000 UTC 18 October–0000 UTC 21 October 2005) quadruply nested–grid (27/9/3/1 km), cloud-permitting prediction of Hurricane Wilma using the Weather Research and Forecasting model (WRF) with the finest grid length of 1 km and the model top of 30 hPa (or at $z$ = 24 km). The 72-h period covers an initial 15-h spinup (referred to as pre-RI), a 21-h RI, and a 36-h weakening (post-RI) stage (Fig. 1b). Results show that (i) the record-breaking RI of Wilma occurs in the presence of high SSTs (in the range of 29°–30°C) and weak VWS (<5 m $s^{-1}$ between 850 and 200 hPa) during RI, and (ii) the WRF predicts about a 28 m $s^{-1}$ increase in $V_{\mathrm{MAX}}$ and an 80-hPa drop in $P_{\mathrm{MIN}}$ during the 21-h RI period, with peak $V_{\mathrm{MAX}}$ = 72 m $s^{-1}$ and $P_{\mathrm{MIN}}$ = 889 hPa. Later, Zhang and Chen (2012, hereafter ZC12) showed that the model predicts an intense warm core in the same layer as the upper-level outflow at the time of peak intensity and then demonstrated that this upper-level warm core is responsible for most of the RI of Wilma. Thus, they hypothesize that (i) the detrainment of CBs in the eyewall accounts for the formation of such an upper-level warm core and (ii) the upper divergent outflow plays an important role in protecting the warm core from ventilation by environmental flows.

In this paper, we delve deeply into both external and internal processes leading to the RI of Hurricane Wilma (2005) in terms of surface pressure falls. This will be done mostly using the 72-h model prediction data, as presented by Chen et al. (2011), unless otherwise mentioned. The objectives of this paper are to examine (i) the upper-level warm-core and flow structures, and their roles in the intensity changes of Wilma in more detail than those presented in ZC12; (ii) the spatial distribution and evolution of CBs and their roles in the formation of the upper-level warm core; and (iii) the dependence of CB activity, the upper-level warm core, and RI on the warmth of SSTs. The next section presents the vertical structures and evolution of the warm core, in relation to the upper-level flow, and its importance in causing the intensity changes of Wilma. Section 3 shows the statistical characteristics of CBs and their structural variations during the pre-RI and RI stages of Wilma. Section 4 portrays the roles of CBs in the formation of the upper-level warm core. Section 5 shows how CBs and RI depend critically on the warmth of SSTs through

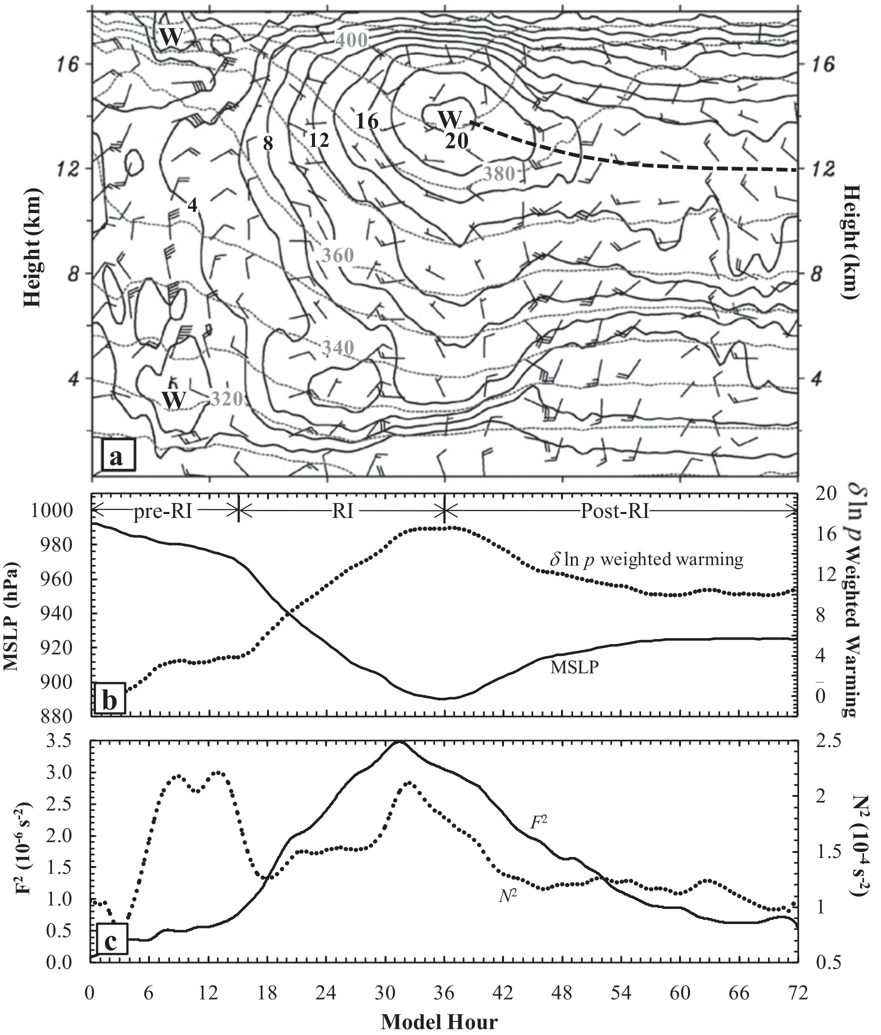

FIG. 1. (a) Time–height cross section of $T'(z, t)$ (solid lines; interval = 2°C), superposed with $\theta$ (dashed lines; interval = 10 K) and storm-relative flows (a full barb is 5 m $s^{-1}$), at the eye center from the 72-h prediction of Hurricane Wilma (2005) at the 3-km resolution and 30-min interval, where $T'(z, t)$ is defined with respect to the 1000 km × 1000 km $\overline{T}(z)$ at the model initial time. (b) Time series of $P_{\mathrm{MIN}}$ (hPa, solid) that is obtained by integrating the hydrostatic equation from the model top downward using the total temperature [i.e., $\overline{T}(z) + T'(z, t)$] and of the $\delta$ln$p$-weighted warming (°C, dotted), defined as $\int T'\delta(\ln p)/\ln(p_{12}/p_{18})$, where $p_{12}$ and $p_{18}$ are the pressures at $z = 12$ and 18 km, respectively. (c) Time series of the layer-averaged $F^2$ (solid) and $N^2$ (dotted) between 14 and 16 km within a radius of 60 km centered in the eye (see text).

a sensitivity simulation in which SSTs are reduced by 1°C.

## 2. Impact of the upper-level warm core and flows

Figure 1 shows the time–height cross section of perturbation temperatures $T'(z, t)$ with respect to the area-averaged vertical temperature profile at the model initial time in relation to the time series of $P_{\mathrm{MIN}}$, the potential temperature $\theta$, and storm-relative flows (SRFs) all at the eye center. Initially, the hurricane vortex has a warm core of 4°–5°C centered near $z = 7$ km. Because of the influence of moderate VWS (i.e., 5–7 m $s^{-1}$) and midlevel dry intrusion, Wilma exhibits a southeastward-tilted partial eyewall pattern during the early pre-RI stage (Chen et al. 2011). Thus, we see two warming centers during the first 6–12 h of integrations: one is located at $z = 4$ km and the other at $z = 12$ km. For the sake of convenience in relating the results shown in Figs. 1a,b, we use the word "warming" to imply a positive temperature change(s) with respect to the initial mean temperature profile in the storm-relative framework. In addition, we use the model hours (i.e., aa:bb, where aa and bb denote the hours and minutes of model integrations, respectively), instead of UTC, to discuss the evolution and structural changes of the model-predicted storm. At 06:00, a shallow upper warming layer of 6°–8°C begins to develop above the deep warming column in the eye. Note that this warming takes place in the lower stratosphere, as indicated by the larger vertical $\theta$ gradient above $z = 16$ km. Note also that the $\theta = 370$–$400$ K layer starts descending at the onset of RI (i.e., 15:00), causing the subsequent intensification of the upper-level warming until reaching the storm maximum intensity at 36:00 (cf. Figs. 1a,b). Since little diabatic heating occurs in the eye, this warming must be associated with the subsidence of lower stratospheric air. During the 21-h RI, the $\theta = 370$ K surface descends from $z = 16$ to 9 km, causing an intense warming column with the peak amplitude of more than 20°C near $z = 14$ km. This peak amplitude is similar to but located at about 2 km higher than that found in early observational studies of LaSeur and Hawkins (1963) and Hawkins and Rubsam (1968). Based on the discussion of ZC12, the different altitudes are hydrostatically consistent because Wilma is a record-intense storm.

The isentropic surfaces begin to climb back after reaching the peak intensity, while the warming core weakens and shifts downward during post-RI, corresponding to the rise in $P_{\mathrm{MIN}}$ of Wilma. As shown in Part I, this timing is consistent with an eyewall replacement cycle (ERC) beginning near 36:00, during which the original eyewall is replaced by an outer eyewall with doubled radii of maximum wind (RMW). The warming core descends to 12 km at 48:00, that is, at a level close to that occurring during pre-RI. It remains at that level until 72:00, which is consistent with the near-steady state of $P_{\mathrm{MIN}}$. The above-mentioned results reveal that the upper-level warming, the inner-core structural changes, and the storm intensity are all closely related. In particular, the RI, rapid weakening, and peak intensity of Wilma coincide well with the steep downward and upward sloping, and the lowest elevation of isentropic surfaces, respectively.

Note the pronounced changes in static stability ($N^2 = g\partial\ln\theta/\partial z$) in the column above the $\theta = 370$ K surface, which resemble in trend the time series of $P_{\mathrm{MIN}}$ (cf. Figs. 1a,b). This implies that the $P_{\mathrm{MIN}}$ falls are closely related to the upper-level warming of stratospheric air. This could be quantified by the $\delta\ln p$-weighted warming that exhibits a 15-h slow increase, followed by a sharp increase at the onset of RI, and decreases after reaching the lowest $P_{\mathrm{MIN}}$ (see the dotted line in Fig. 1b), with its general trends opposite to those of $P_{\mathrm{MIN}}$. ZC12 demonstrate through the hydrostatic equation that the upper-level warming is more efficient than the lower-level warming in causing the RI of Wilma. Without the descent of stratospheric air, $P_{\mathrm{MIN}}$ could only drop 25–40 hPa from its initial intensity during the 72-h prediction (see Fig. 1 in ZC12). Of importance is that the areal and ($z = 14$–$16$ km) layer-averaged $N^2$ decreases and inertial stability $\{F^2 = (f + 2V/r)[f + 1/r\partial(rV)/\partial r]$, where $V$ is the tangential wind and $f$ is the Coriolis parameter$\}$ decreases both sharply about 2–3 h prior to the onset of RI (Fig. 1c). As will be discussed in section 4, these changes in $N^2$ and $F^2$ facilitate the buildup of the upper-level warm core.

Figures 2a,b show the vertical structures of brightness temperature anomaly from Advanced Microwave Sounding Unit (AMSU) observations at two times that are about 3 h after those in Figs. 2c,d during RI and post-RI, respectively. Despite some differences between brightness temperature and temperature, the former can be used as a proxy for the latter to show the upper-level warm core (Kidder et al. 1978; Velden and Smith 1983; Zhu et al. 2002). We see that the warm core was located around 150 hPa or $z = 14$ km at 33:00, which is at the same altitude as that in Fig. 2c. When Wilma entered its post-RI stage, the warm-core altitude was lowered to about 230 hPa, or $z = 11.5$ km, which is 0.5 km lower than that in Fig. 2d. The smaller warm-core amplitude in Fig. 2a may be attributed to a large scanning angle of the AMSU's coarse-resolution measurement. Overall, the AMSU observations substantiate the high altitude of the warm core and its vertical displacement presented in Fig. 1a.

Figures 2c,d also show the relationship between the thermal and flow fields in the core region. The in-plan flow vectors exhibit the typical inward, upward, and outward secondary circulation of a mature TC, which influences the general warming pattern. This is especially true at later stages in the upper outflow layer, where the warming spreads more laterally outward (Fig. 2d). Note that the peak warming core is located in the same layer as the upper-level outflow, for example, the 13–15-km layer during RI (Fig. 2c) and the 11–13-km layer during post-RI (Fig. 2d). The time series of vertical wind profiles in the eye reveals that the upper-level warming magnitudes are correlated with those of the upper-level SRFs (Fig. 1a), suggesting that the divergent outflow tends to protect the warming core from ventilation by environmental flows (ZC12). In contrast, the SRFs during the pre-RI stage are about 10–20 m s$^{-1}$ in a deep layer (i.e., $z = 2$–$18$ km) in the eye, which is consistent with cloud asymmetries under the influence of moderate VWS. Clearly, such intense SRFs tend to prevent the accumulation of warming air in the eye by ventilating it into the environment. Of equal importance is that according to geostrophic adjustment theory

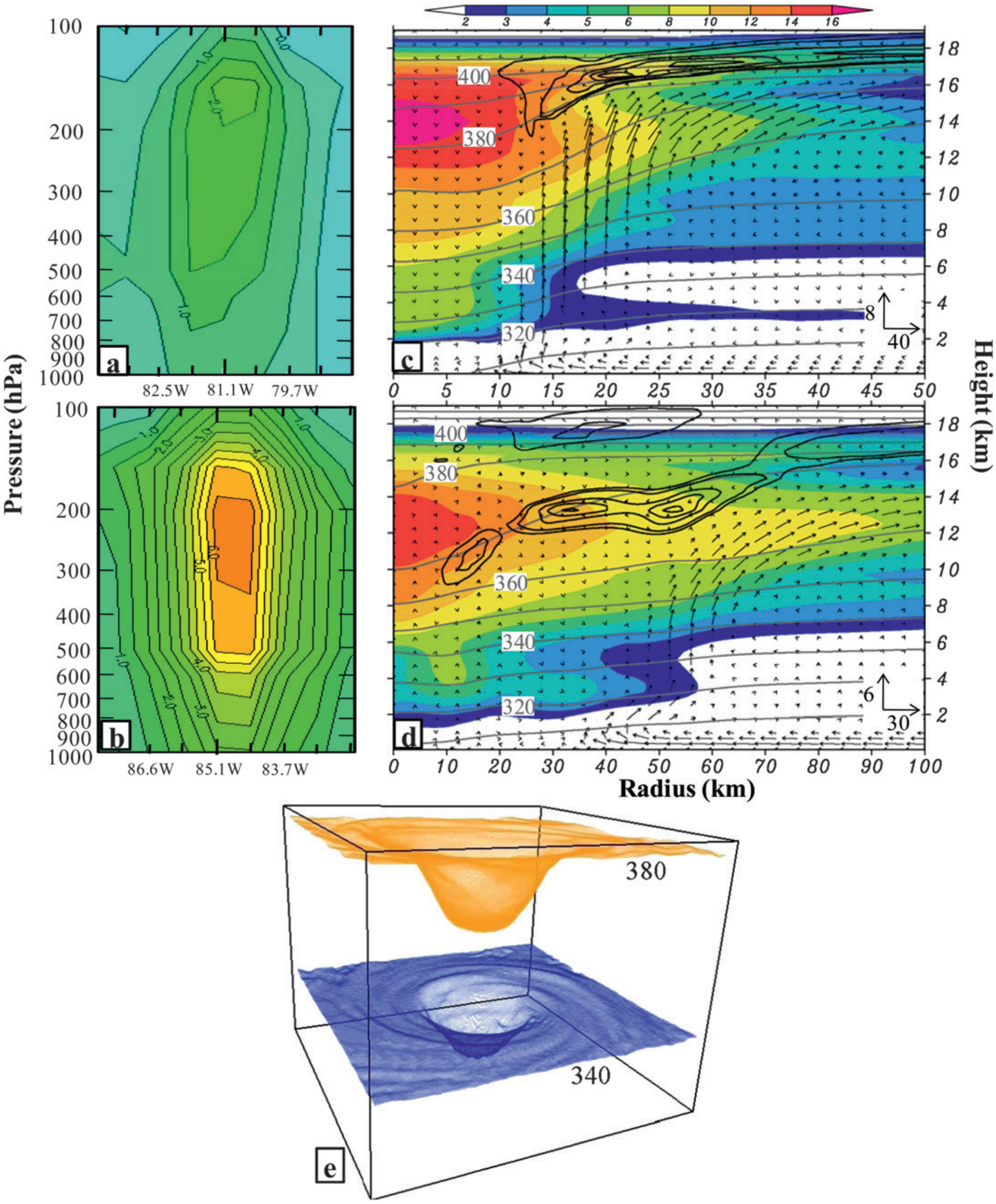

FIG. 2. West–east cross section of the AMSU brightness temperature anomaly (every 0.5°C) at (a) 0859 UTC 19 Oct and (b) 0847 UTC 20 Oct, corresponding to 32:59 and 56:47, respectively. Radius–height cross section of $T'(z, t)$, (shaded) with respect to the 1000 km × 1000 km $\overline{T}(z)$ at the model initial time, superposed with $\theta$ (contours; interval = 10 K), in-plane flow vectors (m $s^{-1}$, scaled by orthogonal arrows; vertical motions are multiplied by 5), and the upper-level radial inflows (contoured at 0.5 m $s^{-1}$) from the (c) 30- and (d) 54-h predictions of Hurricane Wilma (2005). Different radii are given beneath each frame, and different horizontal and vertical motion scales (m $s^{-1}$) are given at the bottom right of each frame. (e) A three-dimensional view of the 380- and 340-K isentropic surfaces in a 100 km × 100 km × 13.5 km (i.e., $z$ = 3.5–17 km) box from the 36-h prediction.

(Blumen 1972), most of the convectively generated mass perturbations tend to be propagated away (more vertically) by high-frequency internal gravity waves at the earlier stages, especially in the lower stratosphere where $N^2$ is high (Fovell et al. 1992), as also indicated in Figs. 1a,c. This will be further discussed in section 4. The upper-level SRFs decrease rapidly to less than 5 m $s^{-1}$ at the onset of RI, and they achieve a nearly calm condition at the time of the peak intensity, confirming the important roles of the upper-level outflow in protecting the warm core from ventilation by the environmental flows (ZC12). The SRFs above 14-km altitude become reintensified after the ERC, which coincides with the weakening of the upper-level warming. Meanwhile, the warming core shifts to a lower layer, as does the upper outflow.

Of interest is the presence of an inflow layer of about 2–3 m $s^{-1}$ originating in the lower stratosphere above the upper outflow layer. It begins to emerge at the time of the eye formation, and later it exhibits more pronounced cyclonic rotation (ZC12), especially near the eye, as a result of absolute momentum conservation. The inflow air could descend isentropically—for example, following roughly the $\theta = 370$ K surface—toward the warm core from the outer region at the radius of more than 100 km (Fig. 2d). Although this has not been documented in any of previous observations, numerous model simulations have shown its existence (e.g., Rotunno and Emanuel 1987; Liu et al. 1999), even in a dry hurricane-like vortex (Mrowiec et al. 2011), but with little attention to the significance of this inflow layer. ZC12 consider this storm-scale inflow layer as being caused by the mass sink in the eye through mass continuity, based on the quasi-balanced vertical motion calculations of Zhang and Kieu (2006).

While the upper-level warming accounts for most of Wilma's deepening, it is essentially the high elevation of the upper outflow layer that makes it a record-breaking storm. Specifically, the elevation of the outflow layer is about 1–2 km higher than that of several intense hurricanes shown by the previous studies, such as Andrew of 1992 (Liu et al. 1999), Dennis of 2005 (Rogers 2010), and Opal of 1995 (Bosart et al. 2000). In the present case, the high outflow elevation benefits from the presence of a higher-than-normal tropopause (at about 100–130 hPa or 16 km) and the development of CBs being tied to warm SSTs. In particular, the maximum potential intensity theory (MPI) of Emanuel (1986, 1988) indicates that a higher-altitude outflow layer tends to boost the thermodynamic efficiency of Carnot's engine that converts sensible and latent heat energy extracted from the underlying warm ocean and ultimately given up in the upper outflow, thereby increasing the storm intensity. In this regard, the eye thermodynamics presented herein are consistent with the eyewall thermodynamics of MPI theory. Moreover, a higher altitude of an inflow layer, residing above the upper outflow layer, can effectively carry the higher-$\theta$ air from the far environment all the way into the hurricane eye, where it descends adiabatically to enhance the warm core due to the presence of little inertial stability.

Figure 2e provides a three-dimensional view of the isentropic surfaces of 380 and 340 K at the time of the peak intensity, that is, 36:00. Both surfaces are funnel shaped in the inner-core region, with their bottoms 5 and 3 km lower than their peripheries, respectively. The different downward displacements of the two surfaces are attributable to locally different static stabilities in the eye. Because the $\theta = 380$ K surface is located above the upper outflow layer with little diabatic effects, the upper-level inflow of stratospheric air must follow closely this isentropic surface, causing strong descending motion and the generation of an intense warming core. In the outer region, the $\theta = 380$ and 340 K surfaces are almost flat with some wavy patterns, and they are associated with gravity waves and spiral rainbands, respectively.

## 3. Statistical characteristics of convective bursts

Before discussing how CBs contribute to the formation of the upper-level warming core, let us examine first some statistical characteristics of CBs. Figure 3 shows the horizontal distribution of CB elements at a few selected times during the pre-RI and RI stages. Because of the large spatial and temporal variabilities of updrafts and their interactions, including merging and splitting, it is often not possible to trace the evolution of individual CBs, except for a few well-defined cases as will be shown later. Thus, CB elements, rather than CBs per se, are statistically examined. We see from Fig. 3 that most CB elements at 06:00 are distributed along a spiral rainband in the southeastern quadrant, which corresponds more or less to the north-northwesterly VWS of about 5 m $s^{-1}$. Although this VWS is relatively weak, it accounts for the asymmetric structures of eyewall convection and CBs at the early stage. The CB band tends to be displaced cyclonically as the storm size shrinks and the eyewall becomes better defined. It moves into the northeastern quadrant 3 h later (Fig. 3b). Starting from 12:00, more CB elements begin to develop in the eyewall (cf. Figs. 3c–e), where the high-equivalent-potential-temperature ($\theta_e$) air and strong convergence are typically located (Liu et al. 1999). By 15:00, almost all CBs take place in the eyewall as it becomes more symmetric (Fig. 3d). Of interest is that the areal coverage of CBs in the inner-core region decreases rapidly as the storm intensifies. This rapid decrease could be attributed partly to the increased stiffness in the eyewall that tends to force moist convection to behave more in a slantwise fashion (Jorgensen 1984; Liu et al. 1997, 1999) and partly to the smaller area occupied by convection in a contracted eyewall. The increased stabilizing effects of the upper-level warming may also help weaken

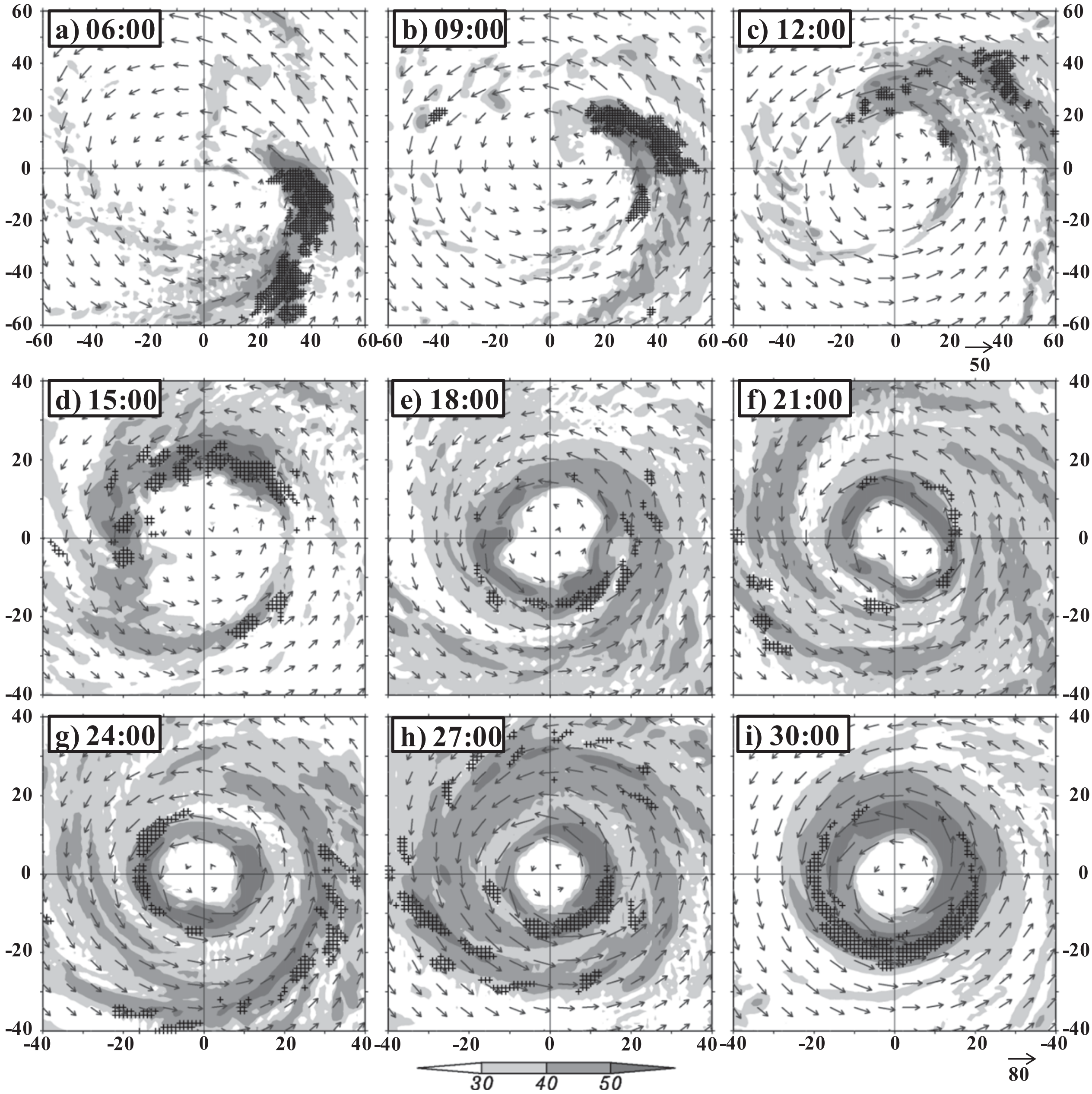

FIG. 3. Horizontal maps of the predicted radar reflectivity (shaded) and storm-relative flow vectors at $z = 1$ km, and CBs (dotted) that are obtained for three time levels at ±5-min intervals. They are plotted at 3-h intervals during the period from (a) 6:00 to (i) 30:00. Note that different subdomain sizes of 120 km × 120 km and 80 km × 80 km, centered at $P_{\mathrm{MIN}}$, with different flow vector scales (m $\mathrm{s}^{-1}$), are used for (a)–(c) and (d)–(i), respectively. Arrows beneath (c) and (i) denote velocity scales for (a)–(c) and (d)–(i), respectively.

updraft intensity. Some CBs could still occur in the outer rainbands due to the presence of large convective available potential energy (CAPE) associated with warm SSTs (e.g., Fig. 3c).

The areal coverage of CBs experiences another cycle of rapid decreases just shortly after the onset of RI (cf. Figs. 3d,e). This occurs as an outer eyewall forms near radius $R = 30$ km during the 18:00–27:00 period, which is more apparent toward the end of that period (cf. Figs. 3g,h), reducing the supply of high-$\theta_e$ air to the inner eyewall. Despite the formation of the outer eyewall, the inner eyewall could still keep contracting with significant CB activity, thus causing little changes in the rate of RI (Fig. 1b). Note that because of the presence of weak

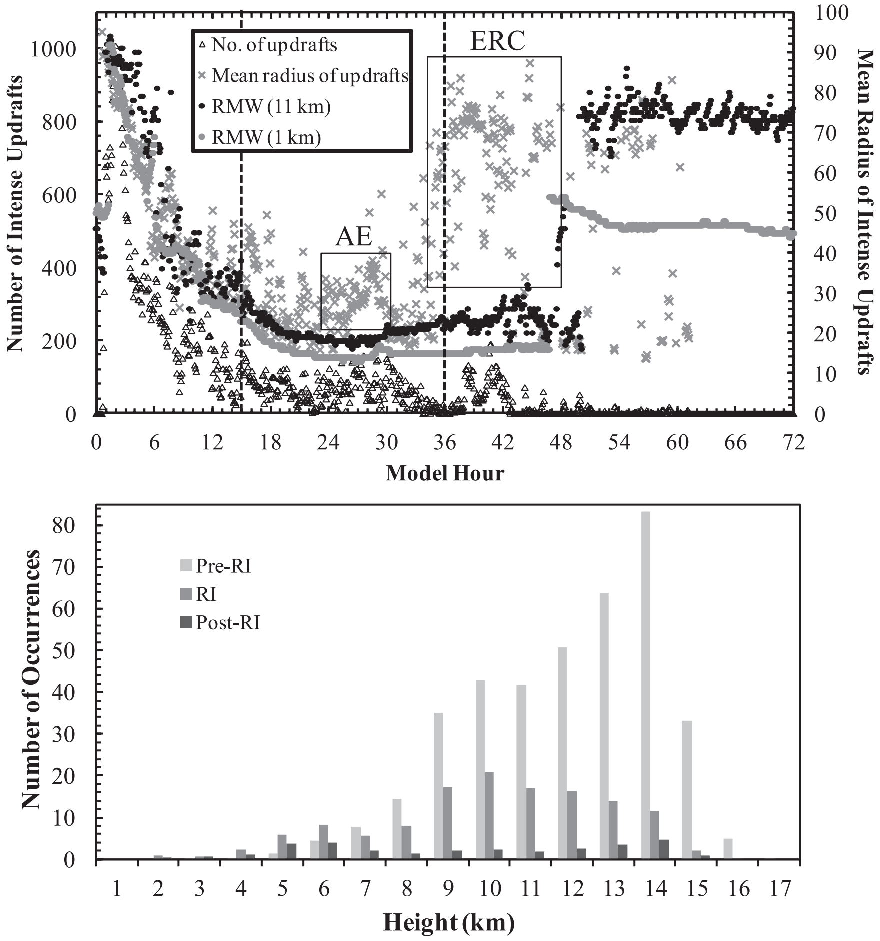

FIG. 4. (a) Time series of the CB activity in terms of the number of total grid columns containing CB elements above 11-km height, the mean radius of the CB-element occurrences, and the RMW at 1- and 11-km altitude. "AE" and "ERC" denote the annulus eyewall and eyewall replacement cycle, respectively. Dashed lines demarcate the pre-RI, RI and post-RI stages. (b) The height distribution of the peak updraft altitudes for the number of their occurrences averaged during the pre-RI, RI, and post-RI stages. In both maps, CB elements are taken within the radius of 100 km from the center from the 72-h prediction of Hurricane Wilma (2005) at the 5-min resolution.

VWS (i.e., $<5$ m s$^{-1}$), cyclonically traveling CBs appear in the different quadrants of the inner and outer eyewalls during RI. The RI is only halted briefly as the two eyewalls merge shortly after 27:00 (Figs. 3h,i, 1b), which is referred to by Chen et al. (2011) as a fictitious eyewall-merging scenario forming an annular eyewall. The CB areal coverage increases substantially, covering more than a semicircle, after the annular eyewall is formed (Fig. 3i). This appears to account for the resumption of RI until reaching the storm's peak intensity at 36:00 (cf. Figs. 3i, 1b). As will be seen in section 5, the storm could continue its RI, even during the double eyewalls stage, because of the continuous development of CBs in the inner eyewall (Figs. 3f–i) that is in turn determined by the underlying warm SSTs.

Figure 4a shows the temporal evolution of CB activity in terms of the number of total grid columns containing updrafts that are at least 15 m s$^{-1}$ above $z = 11$ km. The initial CB activity is determined by large CAPE in the bogussed vortex, and it is peaked after 02:00 with slightly over 1000 CB elements or an equivalent areal coverage of over 1000 km$^2$ at 1-km horizontal grid spacing. The CB activity decreases rapidly after the first 6-h model adjustment, during which rapid contraction occurs, as also shown in Fig. 3. The CB activity maintains at a stable level from the onset of RI to 24:00, followed by an increased CB areal coverage during the formation of the annular eyewall (cf. Figs. 3d–i and 4a).

The CB activity regains its coverage a couple hours after Wilma reaches its peak intensity, that is, during the

ERC, but it occurs mostly in the outer eyewall. Of interest is that the pronounced increases in CB activity produce little changes in $P_{\mathrm{MIN}}$ (cf. Figs. 4a, 1b). This can be explained partly by the low efficiency of diabatic heating in the large-sized eyewall (Hack and Schubert 1986) and partly by the increased ventilation and reduced $F^2$ (Figs. 1a,c). Subsequently, the CB activity remains at a dormant state with occasional spikes between 42:00 and 62:00, corresponding to the weakening stage of the storm (cf. Figs. 4a, 1b). The CB activity is completely absent during the final 10 h (i.e., 62:00–72:00), when the storm enters a steady state. Overall, the evolution of the CB activity over the 72-h period corroborates qualitatively the previous findings that CBs are active preceding and during RI, and that they rarely occur when a TC reaches its quasi-steady state or starts weakening (Heymsfield et al. 2001; Guimond et al. 2010). Here we add that (i) fewer CBs occur during RI than those during pre-RI; and (ii) if the weakening of TCs results from an ERC, then CBs tend to occur in the outer eyewall. Of course, fewer CBs during RI do not mean smaller contributions to the RI of Wilma. Rather, the contributions of CBs to the RI through the upper-level warm core are much greater than those at the earlier stages because of the generation of a balanced cyclonic circulation (with increased $F^2$) in the core, as will be further discussed in the next section.

Figure 4a also shows the mean radius where CB elements take place with respect to the RMWs at $z = 1$ and 11 km. Wilma's eyewall is nearly upright, with only a 3–5-km outward tilt up to $z = 11$ km during pre-RI and RI, but a large outwardly tilt (i.e., about 30 km) after the ERC. Except for the first 1–2-h vortex adjustment, all three radii contract rapidly during the subsequent 12–14-h pre-RI period, and the occurrences of CB elements straddle the RMWs. Note that the CB activity becomes scattered with more CBs located outside the RMW during the 10:00–32:00 period. This scattered CB activity is related partly to its development in spiral rainbands (i.e., for those occurring more than 10 km outward from the RMW) and partly to the outward tilt of CB elements above $z = 11$ km as they overshoot slantwise outward into the lower stratosphere (see Fig. 3 in ZC12). Again, the formation of the annular eyewall accounts for the sharp fluctuations in the radius of CB elements around 27:00. Note also that the RMW at $z = 11$ km increases slightly after 30:00, while the RMW at $z = 1$ km remains constant, implying the more slantwise nature of CB elements and the eyewall. This is consistent with the rapid decrease in CB activity in the inner-core region during the final 6-h RI period. During and after the ERC, a majority of CB elements appear in the outer eyewall, mostly near the RMW at $z = 11$ km, indicating that they slope outward in the same manner as the eyewall.

To examine the likely upward penetration of CBs and their detrainment in the inner-core region, Fig. 4b shows the height distribution of the peak updraft altitudes for the number of their averaged occurrences during the pre-RI, RI and post-RI stages. Note that they are not necessarily all associated with CBs, since the criterion for the peak updrafts of greater than 15 m s$^{-1}$ is not limited to the levels above $z = 11$ km. Despite this relaxed criterion, we still see that the peak updrafts take place mostly in the upper troposphere during pre-RI, with their most preferred altitude occurring at $z = 14$ km in coincidence with the warming-core level. This preferred altitude shifts to 10 km during RI, with another preferred altitude at 6 km where the melting level is roughly located. Nevertheless, a sizeable portion of peak updrafts still occur at $z = 14$ km and above. Two preferred peak updraft levels appear during post-RI: one at 6 km and the other at 14 km; the latter is more associated with CBs in the outer eyewall. Since the peak updraft level denotes roughly the equilibrium level, above which the rising air in an updraft begins to detrain, a higher peak updraft level implies the more likely penetration (with detrainment) of deep convection into the lower stratosphere. Thus, the above-mentioned result confirms further that the warming core at $z = 14$ km results mostly, if not all, from the compensating subsidence of the stratospheric air due to the development of intense CBs during the pre-RI and RI stages.

## 4. Convective bursts and the upper-level warm core

After seeing the statistical characteristics of CBs, we can explore the roles of CBs in the formation of the eye and upper-level warm core. This will be done by examining the upper-level flows and clouds near the onset of RI, when a well-defined warm core and eye begin to form.

### a. Formation of the eye

Figure 5 traces the evolution of four CBs, labeled as ''A,'' ''B,'' ''C,'' and ''D,'' in the inner-core region during the period of 14:35–15:45 through snapshots of the model-predicted outgoing longwave radiation (OLR), superposed with vertical motion at $z = 15$ km. The OLR is calculated using the model-predicted cloud-top temperature, which can be considered as a surrogate for satellite images showing brightness temperature. Note that (i) at 15-km altitude, most updrafts that are weaker than 5 m s$^{-1}$ are filtered; and (ii) CBs in the eyewall with significant updrafts can be well resolved by many CB elements. At 14:35, which is 25 min earlier

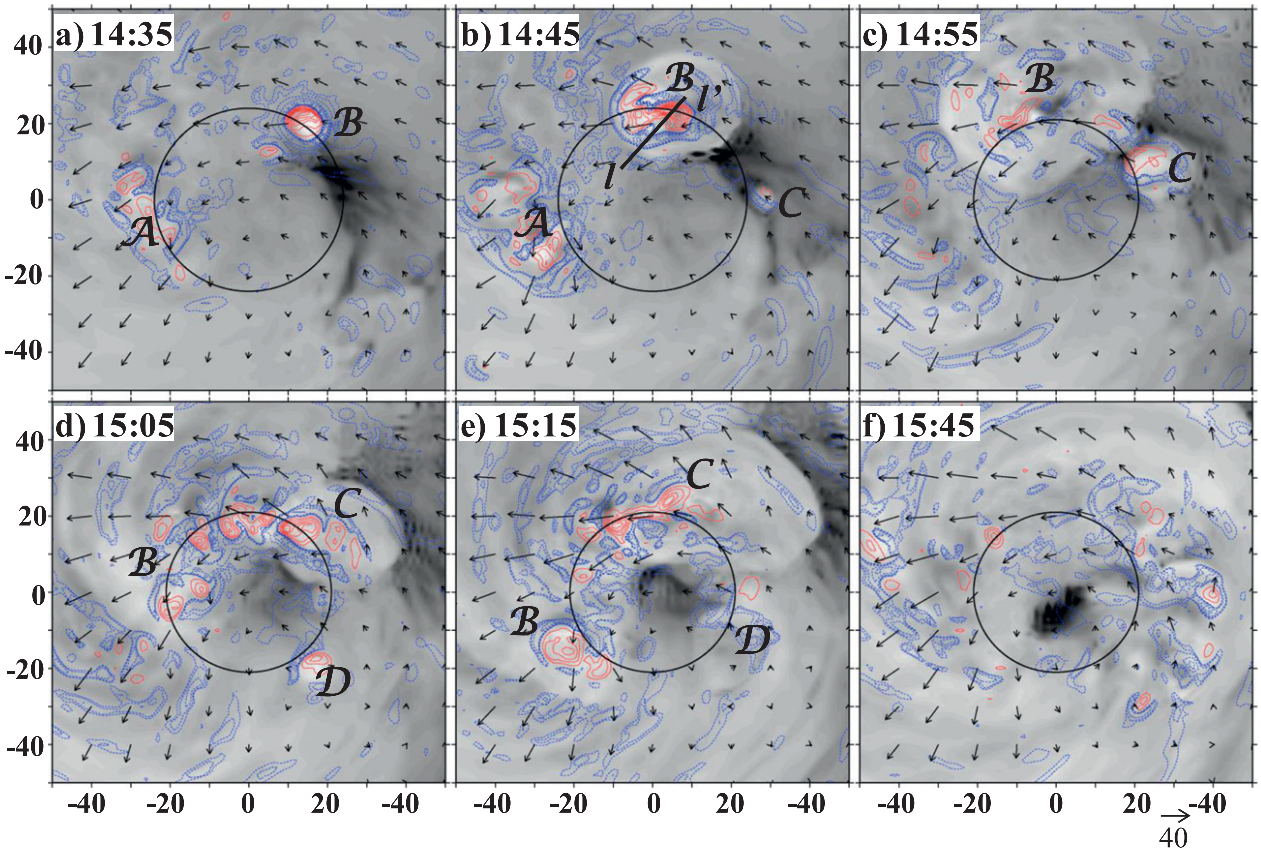

FIG. 5. Horizontal maps of the predicted OLR superimposed with storm-relative flow vectors [see the scale below (f)] and vertical motion (upward/red contours at interval of 5 m $s^{-1}$, downward/blue contours at $-0.5$, $-1$, $-2$, $-4$, $-6$, $-8$, and $-10$ m $s^{-1}$) at $z = 15$ km over the subdomains of 100 km × 100 km, centered at $P_{\mathrm{MIN}}$, that are taken at an interval of 10 min, except for (f) and (g) between which a 30-min interval is used, during the period from (a) 14:00 to (g) 15:45 (i.e., at the onset of RI). The mean RMW at $z = 1$ km is also plotted. Letters A–D are used to trace the evolution of four different convective bursts (see text). Line l–l′ in (b) denotes the location of a vertical cross section used in Fig. 6.

than the map shown in Fig. 3d, two CBs, A and B, are evident around the 1-km altitude RMW (Fig. 5a). CB A, located to the west and slightly outside the RMW, consists of a few scattered updrafts flanked by compensating subsidence, so it has an azimuthal scale of 20–25 km and a width of about 10 km. CB A reaches its maximum coverage near 14:45 and then weakens, leaving its footprints as outward emitting (subsidence/cloud free) wave-like bands. Thus, most of the subsidence warming outside the RMW, where both the SRFs and static stability are large, may be viewed as being dispersed away by both SRFs and high-frequency gravity waves (Figs. 5b–d).

In contrast, CB B displays as a bright spot centered at the RMW with a horizontal scale of about 10 km to the northeast (Fig. 5a). To the southeast of CB B is an extensive cloud-free region that is caused by compensating subsidence from previous CBs, and it will be covered soon by convective clouds from the subsequent CB development. A distinct eye will not form until the onset of RI, that is, 1 h later, when the RMW contracts further (Figs. 5b–f). Collocated with CB B is an intense upward motion as strong as 35 m $s^{-1}$ (see Fig. 6). The size and intensity of this CB are similar to those observed, for example, by Houze et al. (2009), Guimond et al. (2010), and Heymsfield et al. (2001). A further examination of the vertical motion field reveals that this strong updraft results from the merging of two to three updrafts at the lower levels. A similar scenario is also observed by Guimond et al. (2010) in Hurricane Dennis (2005), in which two updrafts merge into a wide one (~5–6 km) with the maximum intensity reaching 20 m $s^{-1}$. Surrounding CB B is a ring of compensating subsidence with magnitudes as strong as 10 m $s^{-1}$ (Fig. 6).

Ten minutes later, the cloud top associated with CB B expands into a blob of some 30 km in diameter as it slowly moves cyclonically along the RMW (Fig. 5b). Its updraft region is now distorted into a bow shape with

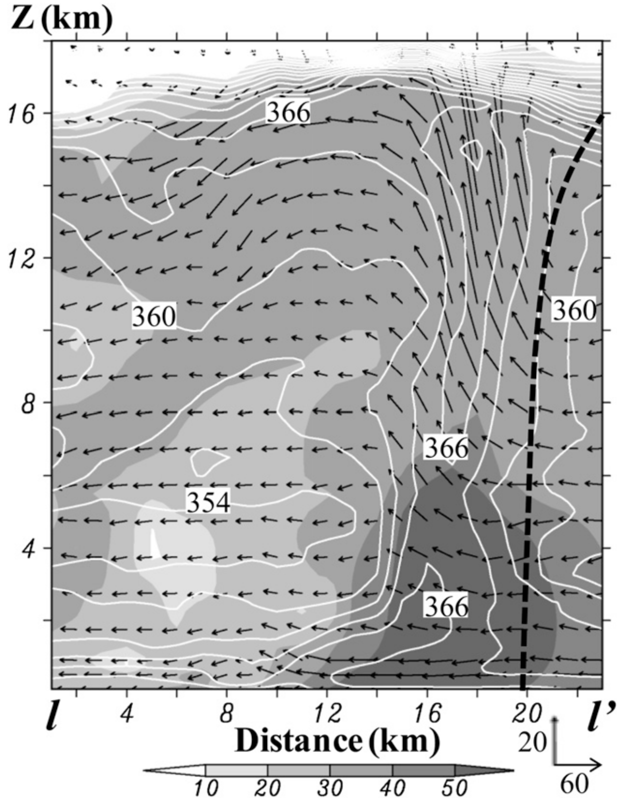

FIG. 6. Vertical cross section of radar reflectivity (dB$Z$, shaded), $\theta_e$ (white solid lines at intervals of 3 K), and in-plane storm-relative flow vectors (m s$^{-1}$, scaled by two orthogonal arrows), taken at 14:45 along line l–l′ in Fig. 5. Thick dashed lines denote the vertical distribution of the local RMW.

two local maxima, and it is surrounded by subsidence with stronger descent occurring inside the RMW. Its cloud top expands rapidly outward to 50–60 km in radius with increased divergence as the peak updraft of CB B decreases in the next 30 min (Figs. 5b–e). Of interest is that three localized updrafts of more than 15 m s$^{-1}$ are spawned along the RMW from the expanding clouds of CB B at 15:05. They are found to grow upward from the lower layers during the previous 30 min, as mentioned in the preceding paragraph.

Another CB, "C," is initiated in the cloud-free region to the southeast of CB B at 14:45 (Fig. 5b). At this time, its peak updraft is only 14 m s$^{-1}$ at $z$ = 13 km and 8 m s$^{-1}$ at $z$ = 15 km, so it does not meet the minimum updraft intensity threshold for a CB until 14:55. Because of its weak intensity, CB C's updraft tilts more outward with height than CB B, as indicated by their central locations with respect to the 1-km height RMW (Fig. 3b). Nevertheless, CB C could produce 30-dB$Z$ radar reflectivity at 15-km altitude at its most intense stage at 15:05 (not shown). The continuous expansion and cyclonic propagation of the CBs, together with the growth of CB C following the evolution of CB B allow the upper-level clouds to wrap around with time, and then a cloud-free eye becomes more evident inside the RMW (Figs. 5c–e); that is, despite that most of the subsidence warming outside the RMW is ventilated away by the strong divergent outflow and high-frequency gravity waves, more subsidence bands begin to take place as lower-frequency propagating gravity waves inside the RMW where $N^2$ is significantly reduced (see Liu et al. 1999; Figs. 1c, 2c,d). This is especially true at 15:05 and 15:15, when the eye starts forming. Clearly, both CB B and CB C make more significant contributions than the other convective elements in the eyewall to the formation of the eye, at least during this early stage of the eye formation.

The fourth discernible intense CB, "D," during the 1-h mapping period is initiated near 15:05 in the southeastern quadrant of the eyewall (Fig. 5d). CB D is the weakest and shortest lived (a traceable period of less than 20 min) among the four CBs, whereas CB B is the strongest with a traceable period of more than 40 min. Figure 5f shows a more symmetric cloud pattern with a small but clear eye at the vortex center, corresponding closely to the onset of RI. Unlike the earlier cloud-free region (e.g., at 14:35), the eye remains cloud free with nearly calm winds at the center throughout the rest of the 72-h integration. The evolution of clouds from an asymmetric to a symmetric pattern and the subsequent eye formation as a result of CB episodes have also been documented by Guimond et al. (2010) in the observational analysis of Hurricane Dennis (2005).

As an example, Fig. 6 shows the vertical structures of CB B at 14:45. This CB has a radial scale of about 10 km, with peak updraft of 35 m s$^{-1}$ at $z$ = 15 km, radar reflectivity of greater than 35 dB$Z$ at $z$ = 16 km, and a cloud top reaching 17.5-km height into the lower stratosphere. In addition, its updraft core takes place slightly inside the local RMW, where the highest-$\theta_e$ air is located. Of relevance is that this upper-level massive updraft is flanked by divergent outflows or cloud detrainment, as indicated by both SRF vectors and reflectivity "anvils," with the inward branch descending from 17-km altitude into the eye. The subsidence could extend radially to the eye center and down to about 10-km altitude, which is consistent with the collectively generated warming (and drying) shown in Figs. 1, 2. In this context, CBs after 15:00 must play an important role in generating an intense upper-level warm core for the RI of Wilma, especially when considering the continuous contraction of the eyewall (see Figs. 1, 3, 7). Note that this subsidence tends to propagate cyclonically downstream in the eye, as shown by Liu et al. (1999) and Fig. 7 herein. This is why the vertical cross section used

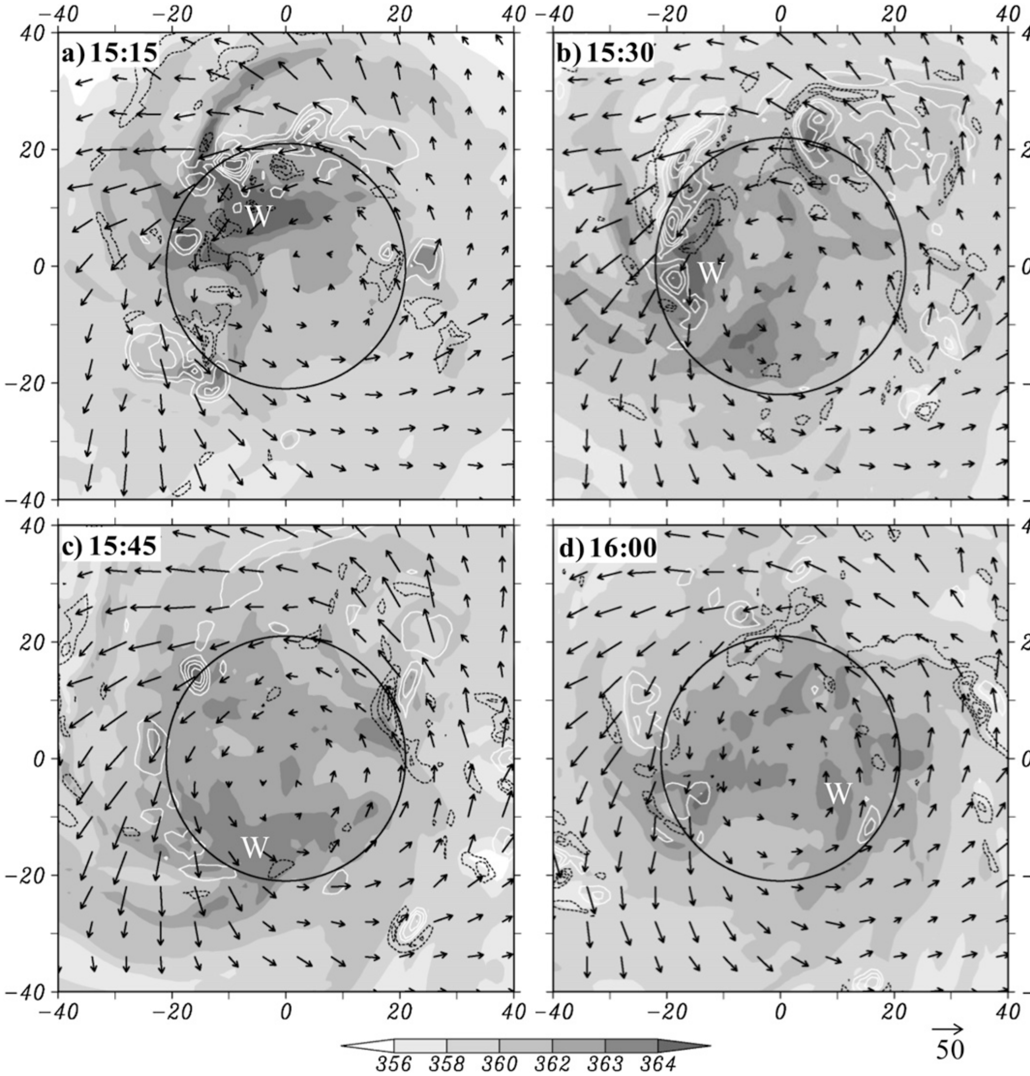

FIG. 7. Horizontal distribution of $\theta$ (shaded) and vertical motion (upward/white contours at an interval of 5 m s$^{-1}$, downward/black contours at an interval of $-2$ m s$^{-1}$), superposed with storm-relative flow vectors [see the scale below (d)], over the subdomains of 80 km × 80 km, centered at $P_{\mathrm{MIN}}$, that are taken at a 15-min interval at $z = 14$ km during the period from (a) 15:15 to (d) 16:00 (i.e., at the onset of RI). Letter W is used to trace the evolution of a warm spot discussed in the text. The mean RMW at $z = 1$ km is also plotted.

in Fig. 6 is not taken radially. ZC12 show more clear evidence of the stratospheric subsidence from a CB occurring at 30:00, when the balanced warming core becomes intense with steep-tilted isentropic surfaces (but weak $N^2$).

### b. Development of the upper-level warm core

Figure 7 shows the horizontal distribution of $\theta$ (shaded) superposed with the vertical motion and SRF, at 15-min intervals near the onset of RI, and it is taken at $z = 14$ km, where the upper outflow layer is located. In general, we see a warm core secured inside the RMW, where weak rotational flows are present, and divergent outflows spreading warmer air outward into the outer region, especially after a more symmetric cyclonic circulation is developed (cf. Figs. 7d, 3d). Of importance is that more significant warm anomalies associated with CBs appear inside the RMW, with little influence from environmental flow. This confirms further the important roles of the upper outflow in protecting the warm core from ventilation by environmental flows. At this stage, energy dispersion by gravity waves is much smaller in the core region (Fig. 1c) than that in the outer region and higher up due to large contrasts in $N^2$ (see Figs. 1a, 2c,d). With little environmental ventilation and energy dispersion, the intensification of the warming core accelerates—for example, from 4°C near the onset of RI to 20°C at the peak storm intensity—causing the more RI of the storm (Fig. 1). We also see from Fig. 7 that the compensating subsidence of CBs in the eyewall could produce 6°–8°C warm anomalies in the eye, which are then cyclonically ''advected'' downstream by weak rotational flows and lower-frequency gravity waves. Figures 7a–d show an example of the evolution of a warm anomaly, denoted by ''W,'' associated with CB C (cf. Figs. 7a, 5e). It can be traced for a period of 45 min, and it is eventually ''trapped'' in the central calm-flow region of the eye, where the mass and wind fields are balanced with large $F^2$ (Fig. 1c). Numerical diffusion also appears to help smooth the warm anomalies.

It is of interest to note that some warm anomalies are collocated with CBs in the eyewall (see Figs. 7a,b), suggesting that the high-$\theta$ air acts as buoyancy facilitating the upward acceleration of air parcels in the CBs, and it accounts for the generation of some upward motion peaks higher up. Such warm anomalies are relatively short-lived, as they tend to be quickly compensated by adiabatic cooling in the CBs. This can be seen from Figs. 7b,c, showing that the $\theta \geq 364$ K mass in the eyewall disappears in 15 min after the weakening of the associated CBs.

Given the pronounced CB activity and subsidence warming at the early pre-RI stage, why cannot the upper-level warm core form until the onset of RI, that is, 15:00? Although we have used Fig. 1a to indicate the ventilation effect of environmental flows, Fig. 8 reveals that this could be attributed to (i) the absence of a symmetric outflow layer aloft and (ii) the presence of more pronounced gravity wave activity during pre-RI, as also shown by large $N^2$ and small $F^2$ in Fig. 1c. Specifically, Fig. 8 shows strong divergent outflows emanating from CBs with little cyclonic flows. Most of the subsidence warming produced by the CBs will be advected away into the outer region and dispersed vertically by gravity waves, as shown by Fovell et al. (1992). For example, the warm air generated by the CBs in the northern semicircle at 11:25 is advected outward, except in the southeastern quadrant, and dispersed vertically by gravity waves. Thus, only a small amount of the warming, occurring in the eye where static stability becomes small, could contribute to a balanced wind field (cf. Figs. 8a,b). This is in significant contrast to the warming scenario associated with the organized cyclonic flow in the eye after the onset of RI (cf. Figs. 7, 8). Of course, this by no means implies that the CB-induced warming during pre-RI does not contribute to the subsequent RI of Wilma, but it indicates that an increase in the upper-level warm core also requires the generation of a corresponding cyclonic flows (or increased $F^2$), based on the thermal wind relation. In fact, the development of CBs during pre-RI plays a vital role in leading to the establishment of such a balanced flow aloft, allowing most warming air to be trapped in the core region in the absence of strong VWS or SRFs.

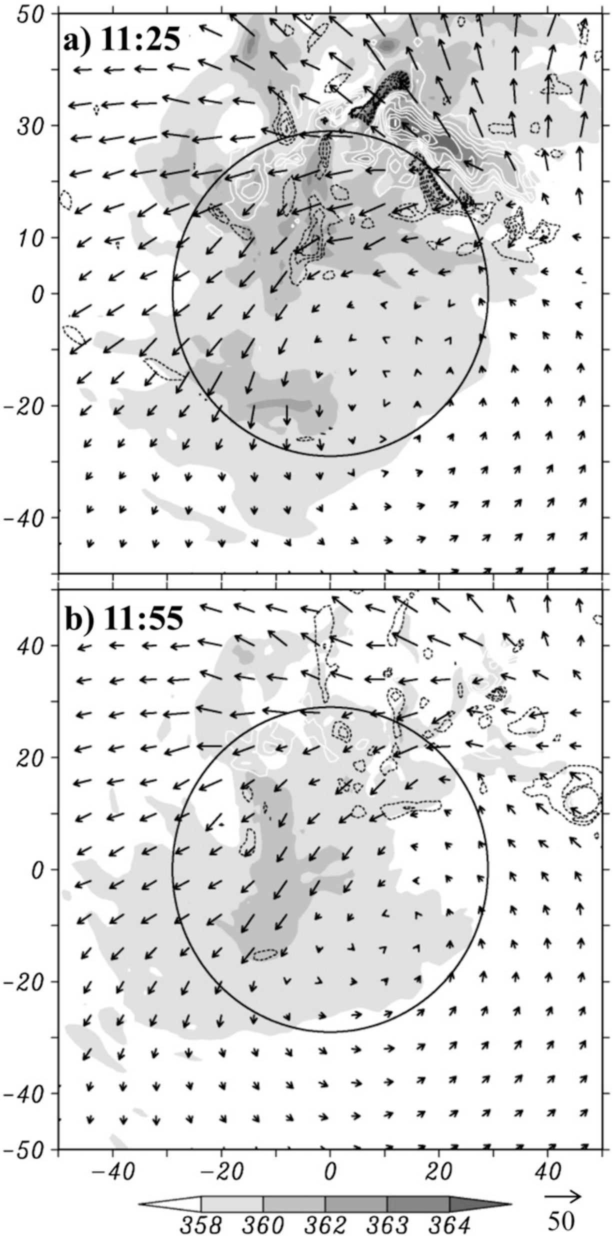

FIG. 8. As in Fig. 7, but for the model integration at (a) 11:25 and (b) 11:55.

## 5. Convective bursts and sea surface temperatures

As mentioned in section 1, previous studies have found that the RI of TCs is associated with warm SSTs

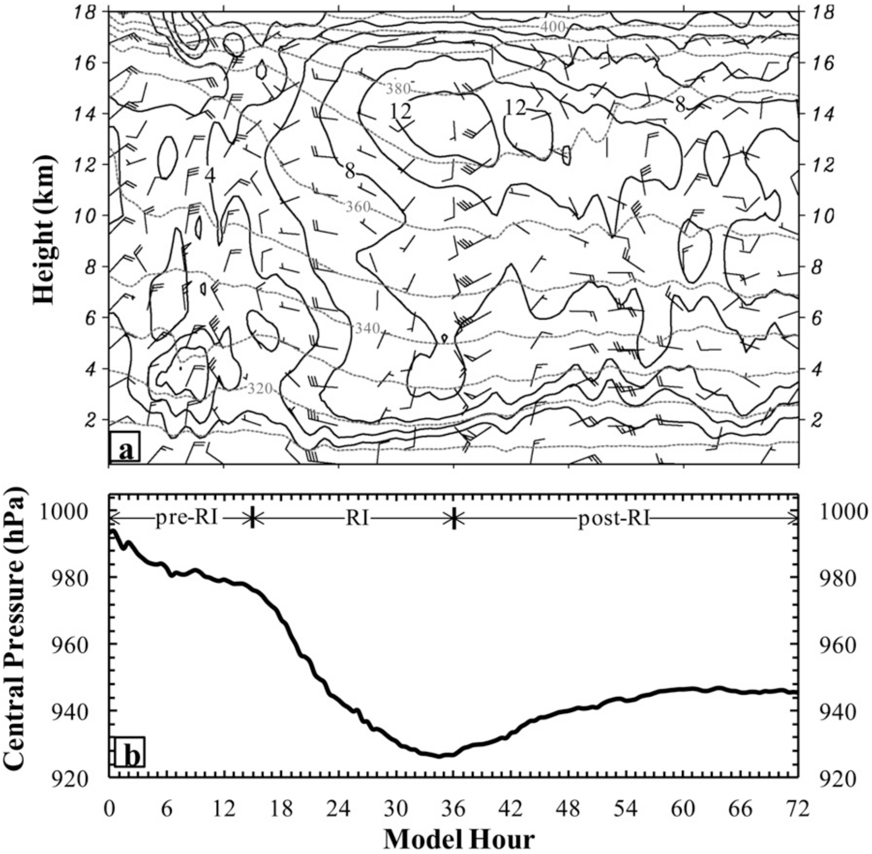

FIG. 9. As in Figs. 1a,b, but for the SST-1 run at the 30-min resolution. The $\delta \ln p$-weighted warming is not plotted.

and active CBs. However, little has been discussed in the literature about their relationship. In this section, we show that CB activity depends critically on the warmth of SSTs, thereby determining the RI rate of Wilma. To this end, a sensitivity simulation is conducted, in which SSTs are reduced by 1°C at every ocean point (SST-1) while holding all the other parameters identical to the control run (CTL) presented in Chen et al. (2011). Despite this reduction, SSTs in the area of interest are still in the range of 28°–29°C.

Figures 9a,b show the time–height distribution of the warming core and the time series of $P_{\mathrm{MIN}}$ of the SST-1 run, respectively. The modeled track of the SST-1 storm is close to the CTL predicted (not shown). We see only slight variations in $P_{\mathrm{MIN}}$ and warming-core intensity and structures during the first 15 h, but large differences during the following 21 h and the remaining period between the SST-1 and control runs. The SST-1 storm exhibits a deepening rate of 2.3 hPa $\mathrm{h}^{-1}$ during the period of 15–36 h, with peak $P_{\mathrm{MIN}}$ = 926 hPa at 36:00. Although this deepening rate still qualifies it as an RI storm, its peak and final intensities are 37 and 20 hPa weaker than the CTL storm, respectively. We have performed several SST sensitivity experiments and found that the storm will no longer intensify when SSTs in the CTL run are reduced by 2.5°C (not shown). Of particular relevance is that the upper-level peak warming core in SST-1 is about 8°C weaker and located about 1 km lower than that of the CTL storm (cf. Figs. 1a, 9a). Both the weaker warm-core intensity and the lower elevation are consistent with the much reduced descent of air from the stratosphere (and weaker $P_{\mathrm{MIN}}$ as well).

Clearly, the above-mentioned results are not surprising, based on the wind-induced surface heat exchange (WISHE) theory that was first discussed by Ooyama (1969) and later clarified by Emanuel (1986, 1991) and Rotunno and Emanuel (1987). However, the WISHE theory does not relate the roles of SSTs in RI to the efficiency of the upper-level warm core. Figure 10 shows the importance of CBs in relating SSTs to the upper-level warm core and RI of Wilma. With the colder SSTs specified, there are fewer CB elements at most times developed during the RI stage, and no CB activity occurs afterward in the inner region. The isentropic surfaces in

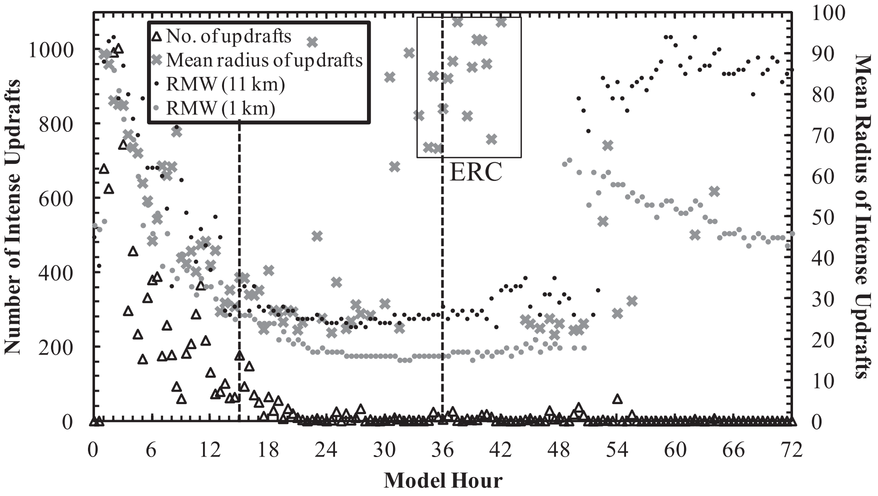

FIG. 10. As in Fig. 4a, but for the SST-1 run at the 30-min resolution.

the lower stratosphere descend much less downward, for example, the $\theta$ = 380-K surface displaces to $z$ = 15 km compared to $z$ = 12 km in CTL (cf. Figs. 10, 1a). This conforms to the generation of a weak upper-level warming core (Fig. 9a). It follows that colder SSTs tend to reduce convective instability and CAPE, precluding deep convection from penetrating as deep into the lower stratosphere. Despite all of the above, the model still generates the ERC during the 30–42-h period, though with few CBs (cf. Figs. 10, 4a). But the SST-1 run does not produce an annulus eyewall (AE) prior to the storm's maximum intensity as in the CTL run.

One may note, however, that there are still many CB elements occurring in the SST-1 run during pre-RI (Fig. 10), albeit less than those in the CTL run. This is apparently caused by the preexistence of high CAPE in the model initial conditions, especially in the bogussed vortex, as mentioned before, so the impact of the specified colder SSTs is delayed for about 20 h. Ideally, the SST-1 run should be initialized 24 h earlier—that is, at 0000 UTC 17 October—which would allow the model atmosphere to be reasonably adjusted for the specified colder SSTs. We may speculate that this procedure would result in a further weakened storm. Nevertheless, this result is consistent with our earlier findings that most CB-induced warming at the earlier stages tends to be propagated away from the inner-core region by high-frequency gravity waves, in addition to the ventilation effects of SRFs. This result indicates from another angle that the CB-induced subsidence warming in the CTL storm appears to contribute more efficiently to the upper-level warm core after a balanced upper cyclonic circulation is established prior to the onset of RI (Fig. 1c).

## 6. Summary and conclusions

In this study, the importance of the upper-level warming core and flow structures, CBs, and warm SSTs in the RI of TCs (in terms of surface pressure falls) is examined using 72-h nested-grid, cloud-permitting predictions of Hurricane Wilma (2005) with the finest grid size of 1 km. Results show that an upper-level warming core (at $z$ = 14 km) forms, in coincidence with the onset of RI, as a result of the descent of stratospheric air in the presence of weak SRFs aloft. Such a high-altitude warming core conforms to the vertical cross sections of AMSU observations. The descent of stratospheric air results from the upper-level detrainment of CBs occurring inside the low-level RMW, where higher-$\theta_e$ air is located. The associated subsidence warming does not become effective until an organized upper-level outflow is established with a weak cyclonic circulation and decreased $N^2$ in the eye. Because of mass continuity, a thin cyclonic radial inflow layer, located above the upper-level outflow layer, is induced by the mass sink and lower pressure in the eye. This inflow air can be isentropically traced to the peak warming core inside the upper-level outflow layer. The importance of the upper-level warming core in RI is consistent with the eyewall thermodynamics of MPI. In the present case, the high altitude of the warming core also benefits from the presence of a higher-than-normal tropopause.

It is shown that CBs, characterized with a radial scale of about 10 km and an azimuthal scale of 10–20 km, have peak updrafts and precipitation tops as high as 11–15-km altitude that are typically flanked by intense subsidence and divergent outflows aloft. It is found that more CBs take place in the inner-core regions prior to the onset of RI, and that their areal coverage decreases rapidly as the storm contracts and reaches a stable level during RI. Results indicate that most of the CB-induced subsidence warming during pre-RI tends to be propagated away by large SRFs and higher-frequency gravity waves, and that it appears to contribute more efficiently to the upper-level warm core after a balanced upper-cyclonic circulation is established near the onset of RI. The intensification of the warm core accelerates, leading to the RI of the storm. It is also shown that considerable CB activity could still occur in the outer eyewall as the storm weakens rapidly as a result of the ERC, suggesting that CBs also play an important role in the contraction of the outer eyewall and the subsequent intensification of the storm through the generation of another upper-level warming core.

The relationship between the development of CBs and SST is examined through a sensitivity simulation of reduced SSTs. Results show that the use of 1°C colder SSTs as the bottom boundary condition results in the development of far fewer CBs during RI, and the generation of a lower-elevated and much weaker warming core, with much less descent of the stratospheric air. As a result, the model produces a storm that is more than 37 hPa weaker than the control storm at their peak intensities. This result suggests that the RI of TCs is determined by SSTs (and other favorable environmental conditions) through the WISHE process and the active development of CBs in the inner-core region that can penetrate into high altitudes. Thus, we may conclude that significant CB activity in the inner-core region in the present case is an important ingredient in generating an intense upper-level warm core that is hydrostatically more efficient to the RI of TCs, given all the other favorable environmental conditions. Based on the above-mentioned results, we recommend that more attention should be paid to the upper-tropospheric flows, rather than just VWS in the typical 850–200-hPa layer, in order to reasonably predict the RI of TCs.

*Acknowledgments.* We wish to thank three anonymous reviewers for their constructive comments, and Chris Velden for kindly providing the AMSU measurements associated with Hurricane Wilma (i.e., Figs. 2a,b) that have helped strengthen the presentation of our modeling results. The model integration was completed on NOAA's NJET supercomputer through the Hurricane Forecast Improvement Program. This work was supported by NASA Grants 1284085 and NNX12AJ78G, and NSF Grant ATM0758609.

## REFERENCES

Blumen, W., 1972: Geostrophic adjustment. *Rev. Geophys.,* **10,** 485–528.

Bosart, L. F., W. E. Bracken, J. Molinari, C. S. Velden, and P. G. Black, 2000: Environmental influences on the rapid intensification of Hurricane Opal (1995) over the Gulf of Mexico. *Mon. Wea. Rev.,* **128,** 322–352.

Chen, H., D.-L. Zhang, J. Carton, and R. Atlas, 2011: On the rapid intensification of Hurricane Wilma (2005). Part I: Model prediction and structural changes. *Wea. Forecasting,* **26,** 885–901.

Emanuel, K. A., 1986: An air–sea interaction theory for tropical cyclones. Part I: Steady-state maintenance. *J. Atmos. Sci.,* **43,** 585–604.

——, 1988: The maximum intensity of hurricanes. *J. Atmos. Sci.,* **45,** 1143–1155.

——, 1991: The theory of hurricanes. *Annu. Rev. Fluid Mech.,* **23,** 179–196.

Fierro, A. O., and J. M. Reisner, 2011: High-resolution simulation of the electrification and lightning of Hurricane Rita during the period of rapid intensification. *J. Atmos. Sci.,* **68,** 477–494.

Foley, G., 1998: A marked upper tropospheric temperature anomaly observed by an aircraft near a thunderstorm over inland Western Australia. *Aust. Meteor. Mag.,* **47,** 321–326.

Fovell, R. G., D. R. Durran, and J. R. Holton, 1992: Numerical simulations of convectively generated stratospheric gravity waves. *J. Atmos. Sci.,* **49,** 1427–1442.

Gentry, R. C., T. T. Fujita, and R. C. Sheets, 1970: Aircraft, spacecraft, satellite, and radar observations of Hurricane Gladys, 1968. *J. Appl. Meteor.,* **9,** 837–850.

Gray, W. M., 1998: The formation of tropical cyclones. *Meteor. Atmos. Phys.,* **67,** 37–69.

Guimond, S. R., G. M. Heymsfield, and F. J. Turk, 2010: Multiscale observations of Hurricane Dennis (2005): The effects of hot towers on rapid intensification. *J. Atmos. Sci.,* **67,** 633–654.

Hack, J. J., and W. H. Schubert, 1986: Nonlinear response of atmospheric vortices to heating by organized cumulus convection. *J. Atmos. Sci.,* **43,** 1559–1573.

Hawkins, H. F., and D. T. Rubsam, 1968: Hurricane Hilda, 1964. II: Structure and budgets of the hurricane core on October 1, 1964. *Mon. Wea. Rev.,* **96,** 617–636.

——, and S. M. Imbembo, 1976: The structure of a small, intense hurricane—Inez 1966. *Mon. Wea. Rev.,* **104,** 418–442.

Heymsfield, G. M., J. B. Halverson, J. Simpson, L. Tian, and T. P. Bui, 2001: ER-2 Doppler radar investigations of the eyewall of Hurricane Bonnie during the Convection and Moisture Experiment-3. *J. Appl. Meteor.,* **40,** 1310–1330.

Hirschberg, P. A., and J. M. Fritsch, 1993: On understanding height tendency. *Mon. Wea. Rev.,* **121,** 2646–2661.

Holland, G. J., 1997: The maximum potential intensity of tropical cyclones. *J. Atmos. Sci.,* **54,** 2519–2541.

——, T. D. Keenan, and G. D. Crane, 1984: Observations of a phenomenal temperature perturbation in Tropical Cyclone Kerry (1979). *Mon. Wea. Rev.,* **112,** 1074–1082.

Holliday, C. R., and A. H. Thompson, 1979: Climatological characteristics of rapidly intensifying typhoons. *Mon. Wea. Rev.,* **107,** 1022–1034.

Houze, R. A., Jr., W.-C. Lee, and M. M. Bell, 2009: Convective contribution to the genesis of Hurricane Ophelia (2005). *Mon. Wea. Rev.,* **137,** 2778–2800.

Jorgensen, D. P., 1984: Mesoscale and convective scale characteristics of nature hurricanes. Part II: Inner core structure of Hurricane Allen (1980). *J. Atmos. Sci.,* **41,** 1287–1311.

Kaplan, J., and M. DeMaria, 2003: Large-scale characteristics of rapidly intensifying tropical cyclones in the North Atlantic basin. *Wea. Forecasting,* **18,** 1093–1108.

Kelley, O. A., J. Stout, and J. B. Halverson, 2004: Tall precipitation cells in tropical cyclone eyewalls are associated with tropical cyclone intensification. *Geophys. Res. Lett.,* **31,** L24112, doi:10.1029/2004GL021616.

Kidder, S. Q., W. M. Gray, and T. H. Vonder Haar, 1978: Estimating tropical cyclone central pressure and outer winds from satellite microwave data. *Mon. Wea. Rev.,* **106,** 1458–1464.

LaSeur, N. E., and H. F. Hawkins, 1963: An analysis of Hurricane Cleo (1958) based on data from research reconnaissance aircraft. *Mon. Wea. Rev.,* **91,** 694–709.

Liu, Y., D.-L. Zhang, and M. K. Yau, 1997: A multiscale numerical study of Hurricane Andrew (1992). Part I: Explicit simulation and verification. *Mon. Wea. Rev.,* **125,** 3073–3093.

——, ——, and ——, 1999: A multiscale numerical study of Hurricane Andrew (1992). Part II: Kinematics and inner-core structures. *Mon. Wea. Rev.,* **127,** 2597–2616.

Malkus, J. S., and H. Riehl, 1960: On the dynamics and energy transformations in steady-state hurricanes. *Tellus,* **12,** 1–20.

Molinari, J., P. K. Moore, and V. P. Idone, 1999: Convective structure of hurricanes as revealed by lightning locations. *Mon. Wea. Rev.,* **127,** 520–534.

Montgomery, M. T., M. E. Nicholls, T. A. Cram, and A. B. Saunders, 2006: A vortical hot tower route to tropical cyclogenesis. *J. Atmos. Sci.,* **63,** 355–386.

Mrowiec, A. A., S. T. Garner, and O. M. Pauluis, 2011: Axisymmetric hurricane in a dry atmosphere: Theoretical framework and numerical experiments. *J. Atmos. Sci.,* **68,** 1607–1619.

Nolan, D. S., 2007: What is the trigger for tropical cyclogenesis? *Aust. Meteor. Mag.,* **56,** 241–266.

Ooyama, K., 1969: Numerical simulation of the life cycle of tropical cyclones. *J. Atmos. Sci.,* **26,** 3–40.

Price, C., M. Asfur, and Y. Yair, 2009: Maximum hurricane intensity preceded by increase in lightning frequency. *Nat. Geosci.,* **2,** 329–332.

Rappaport, E. N., and Coauthors, 2009: Advances and challenges at the National Hurricane Center. *Wea. Forecasting,* **24,** 395–419.

Reasor, P. D., M. D. Eastin, and J. F. Gamache, 2009: Rapidly intensifying Hurricane Guillermo (1997). Part I: Low-wavenumber structure and evolution. *Mon. Wea. Rev.,* **137,** 603–631.

Rodgers, E. B., W. S. Olson, V. M. Karyampudi, and H. F. Pierce, 1998: Satellite-derived latent heating distribution and environmental influences in Hurricane Opal (1995). *Mon. Wea. Rev.,* **126,** 1229–1247.

——, ——, J. Halverson, J. Simpson, and H. Pierce, 2000: Environmental forcing of Supertyphoon Paka's (1997) latent heat structure. *J. Appl. Meteor.,* **39,** 1983–2006.

Rogers, R., 2010: Convective-scale structure and evolution during a high-resolution simulation of tropical cyclone rapid intensification. *J. Atmos. Sci.,* **67,** 44–70.

——, S. Aberson, J. Kaplan, and S. Goldenberg, 2002: A pronounced upper-tropospheric warm anomaly encountered by the NOAA G-IV aircraft in the vicinity of deep convection. *Mon. Wea. Rev.,* **130,** 180–187.

Rotunno, R., and K. A. Emanuel, 1987: An air–sea interaction theory for tropical cyclones. Part II: Evolutionary study using a nonhydrostatic axisymmetric numerical model. *J. Atmos. Sci.,* **44,** 542–561.

Steranka, J., E. B. Rodgers, and R. C. Gentry, 1986: The relationship between satellite-measured convective bursts and tropical cyclone intensification. *Mon. Wea. Rev.,* **114,** 1539–1546.

Velden, C. S., and W. L. Smith, 1983: Monitoring tropical cyclone evolution with NOAA satellite microwave observations. *J. Climate Appl. Meteor.,* **22,** 714–724.

Zhang, D.-L., and J. M. Fritsch, 1988: Numerical sensitivity experiments of varying model physics on the structure, evolution and dynamics of two mesoscale convective systems. *J. Atmos. Sci.,* **45,** 261–293.

——, and C. Q. Kieu, 2006: Potential vorticity diagnosis of a simulated hurricane. Part II: Quasi-balanced contributions to forced secondary circulations. *J. Atmos. Sci.,* **63,** 2898–2914.

——, and H. Chen, 2012: Importance of the upper-level warm core in the rapid intensification of a tropical cyclone. *Geophys. Res. Lett.,* **39,** L02806, doi:10.1029/2011GL050578.

——, Y. Liu, and M. K. Yau, 2000: A multiscale numerical study of Hurricane Andrew (1992). Part III: Dynamically induced vertical motion. *Mon. Wea. Rev.,* **128,** 3772–3788.

Zhu, T., D.-L. Zhang, and F. Weng, 2002: Impact of the Advanced Microwave Sounding Unit data on hurricane forecasts. *Mon. Wea. Rev.,* **130,** 2416–2432.